Chapter 4

Vanadyl ethylene glycolate ($VO(CH_2O)_2$): an organic-inorganic hybrid for Al^{3+} ion storage

Nandi, S., Yan, Y., Yuan, X., Wang, C., He, X., Li, Y., and Das, S. K. *Solid State Ionics*, 389:116085, 2023.

Vanadyl ethylene glycolate ($VO(CH_2O)_2$): an organic-inorganic hybrid for Al^{3+} ion storage

4.1 Introduction

Vanadium based materials have been studied extensively for multivalent ion storage batteries [1-4]. The multiple oxidation states of vanadium (+2 to +5) can support redox reactions with multi electron transfer. Vanadium oxides, vanadium phosphates and metal/nonmetal vanadates have shown to electrochemically store Zn^{2+} and Mg^{2+} ions [4]. In fact, V_2O_5 was the initial cathode material where reversible Al^{3+} ion insertion in nonaqueous chloroaluminate ionic liquid electrolyte was demonstrated [5]. Thereafter, there were attempts to show Al^{3+} ion insertion/extraction in aqueous electrolytes in V_2O_5 [5-11]. There is a class of vanadium-based hybrid material composed of inorganic and organic components known as vanadyl ethylene glycolate ($VO(CH_2O)_2$), abbreviated as VEG, where Al^{3+} ion storage behavior was not investigated. The crystal structure of VEG resembles a one-dimensional chain which consists of VO_5 square pyramid and chelating ligand ($-OCH_2CH_2O-$). The detailed structural analysis was performed by the group of Whittingham [11]. There are sporadic reports for the investigation of Li^+ and Zn^{2+} ion storage in VEG [12-15]. For example, Wang et al. showed that the Li^+ ion kinetics in VEG could be enhanced significantly by the presence of the organic ligand [12]. It was also demonstrated that VEG maintains specific capacity of 550 $mAhg^{-1}$ at current rate of 1 Ag^{-1} for over 2000 cycles. Li et al. demonstrated the performance of lithium-ion battery with VEG. It was shown that VEG could deliver high specific capacities and a capacity of 477 $mAhg^{-1}$ could be achieved over 200 cycles at a current rate of 60 $mAhg^{-1}$ [13]. Similarly, Nagaraj et al. demonstrated the performance of an aqueous zinc-ion battery with VEG as a cathode material. A discharge capacity of above 100 $mAhg^{-1}$ was obtained over 2000 cycles at a current rate of 4 Ag^{-1} [14]. Furthermore, Li et al. also reported a high storage capacity and good cycling stability for Zn^{2+} ion storage at high current rates [15]. In this chapter, the Al^{3+} ion storage behavior of VEG in aqueous electrolyte is discussed. Vanadyl ethylene glycolate nanorods were synthesized by in-situ deposition on a carbon cloth current collector and, thereby, it makes a binder free electrode. It was revealed that the binder free VEG could significantly improve the electrochemical stability in comparison to pristine VEG with binder due to intimate

contact of the electrode material with the current collector which resulted in reduced charge transfer resistance. The binder free electrode could deliver a stable discharge capacity of 77 $mAhg^{-1}$ over 600 cycles at a high current density of 2 Ag^{-1}, whereas pristine VEG shows negligible specific capacity. The Al^{3+} ion storage mechanism is also demonstrated in detailed based on ex-situ XPS, XRD, Raman spectroscopy and electron microscopy techniques.

4.2 Experimental Section

4.2.1 Materials

Ammonium metavanadate [NH_4VO_3, Sigma Aldrich], Ethylene glycol [$C_2H_6O_2$, Merck] and Ethanol/Distilled water.

4.2.2 Synthesis

Synthesis of $VO(CH_2O)_2$: Pristine $VO(CH_2O)_2$ was prepared using a one-step hydrothermal method as reported in ref. [14]. Briefly, to describe, 0.58 g of NH_4VO_3 was added in 30 ml of ethylene glycol and stirred vigorously for 1 h. Then, the obtained solution was transferred to a Teflon-lined stainless-steel autoclave and maintained at 120 ^oC for 24 h and then cooled down naturally to room temperature. The resulting product was separated, washed with distilled water and ethanol several times, and dried at 90 ^oC for 12 h.

Synthesis of binder free $VO(CH_2O)_2$: For the preparation of binder free $VO(CH_2O)_2$ electrode, few pieces of carbon cloth (14 mm in diameter) were dipped in the above mixture solution and performed the hydrothermal treatment as described above. The binder free electrode was collected after the treatment, washed with distilled water/ethanol for few times and finally dried at 90 ^oC for 12 h and abbreviated as bf-VEG/CC in this work. It is to be noted here that there is no control of mass loading on the binder free electrodes. Therefore, for the estimation of the accurate mass loading, the bare carbon substrates were marked before doing the in-situ synthesis for identification. The weights of these bare substrates were noted down before placing them inside the autoclave. After the synthesis, the weights of these electrodes were again noted. Based on the identification marks, the actual weight was estimated by noting the difference between the weights. The weight of the active material varies from 2.5 mg to 3.5 mg.

4.2.3 Characterization

The material was analyzed using powder X-ray diffraction (Rigaku Miniflex II diffractometer with Cu Kα radiation operated at 30 kV and 15 mA, Raman spectra were recorded on a Renishaw 2000 system using a laser wavelength of 633 nm. The morphologies of the samples were characterized using Field emission electron microscopy (FESEM, ZEISS Supra 40V) and transmission electron microscopy (TEM, JEOL-2010 F). X-ray photoelectron spectroscopy (XPS) analysis was performed by the AXIS Ultra DLD system. Thermogravimetric analysis (TGA) was performed under an air flow (50 ml min^{-1}) and ramping rate of 10 °C min^{-1} with Netzsch STA 449 F3 Jupiter.

4.2.4 Electrochemical analysis

Electrode slurry was prepared by mixing $VO(CH_2O)_2$ powder, carbon black and polyvinylidene fluoride in a weight ratio of 7:2:1 using N-methyl-2-pyrrolidone solvent. The slurry was drop cast on pristine carbon cloth (purchased from Fuel cell store, USA, ELAT hydrophilic, Product code: 1591002, 14 mm in diameter) abbreviated as VEG/C and dried at 90 ^oC for 12 h.

Cyclic voltammetry (CV) and galvanostatic discharge/charge experiments were conducted in a conventional three-electrode electrochemical glass cell where Pt electrode and Ag/AgCl electrode were used as the counter and reference electrodes, respectively. The used electrolyte was 1 M $AlCl_3$ unless otherwise specially stated. The discharge/charge and CV experiments were performed in a voltage range of -0.3 to 1 V (vs. Ag/AgCl). Electrochemical impedance spectra (EIS) were recorded in frequency range of 1 mHz-200 kHz at 10 mV signal amplitude. All the electrochemical tests were performed at room temperature (25 ^oC).

4.3 Results and Discussion

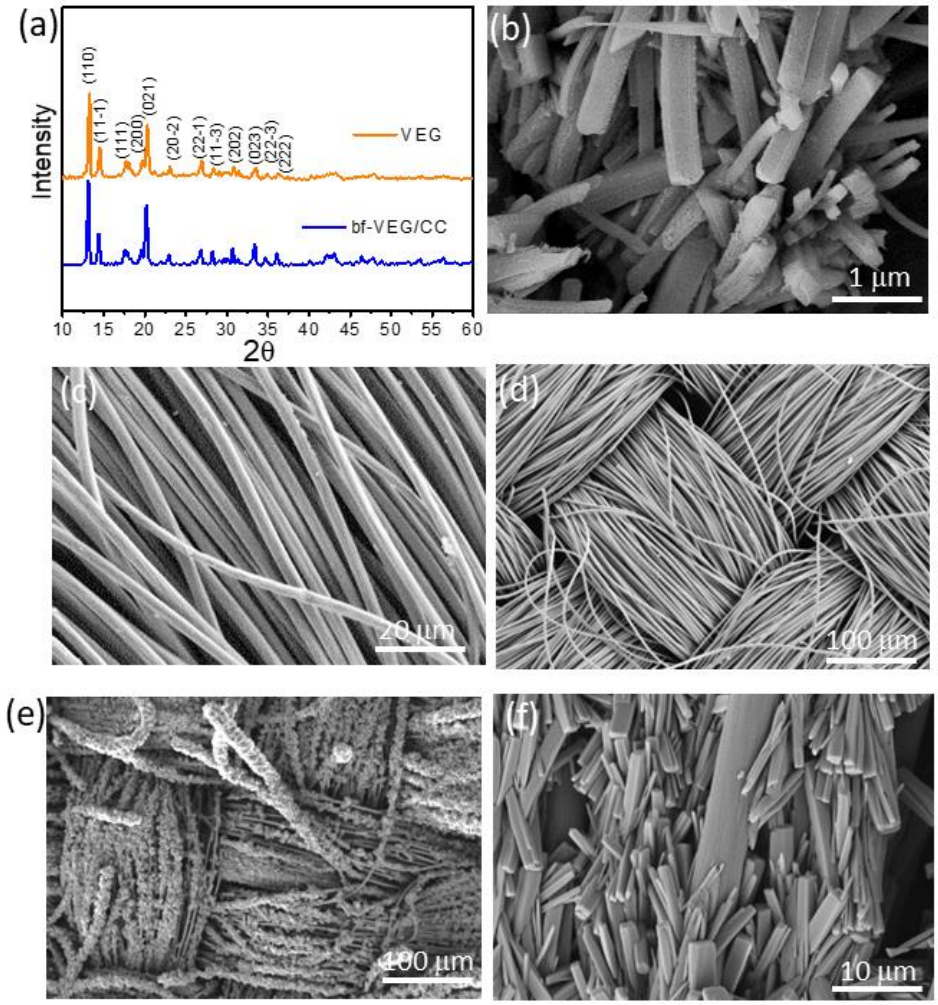

Figure 4.1 (a) XRD patterns, and SEM images of (b) VEG nanorods, (c-d) pristine carbon cloth, and (e, f) bf-VEG/CC.

VEG nanorod was synthesized using a one-step glycothermal method [14]. Binder free VEG electrodes were also glycothermally prepared by growing in-situ VEG nanorods on plasma treated carbon cloth substrate. The carbon cloth was treated with oxygen plasma for 20 min in order to improve hydrophilicity and electrolyte wettability on the surface of the carbon cloth. Figure 4.1a shows the XRD patterns of the VEG nanorods and bf-VEG/CC. It could be seen that the diffraction peaks are mostly matching with the monoclinic crystal phase of VEG with a space group *C*2/*c* (JCPDS no. 49-2497) for both the synthesized products. Figure 4.2b shows the Field emission scanning electron microscope (FESEM) image of the synthesized VEG and it clearly indicates formation of nanorods. Figure 4.1 (c-d) shows the FESEM image of pristine carbon cloth. Figure 4.1(e-f) shows the FESEM images of binder free VEG

nanorods on carbon cloth (abbreviated as bf-VEG/CC). FESEM image of VEG nanorods coated on carbon cloth using PVDF as binder (abbreviated as VEG/CC) is also shown in Figure 4.2a. The carbon cloth is composed of micron size carbon fibers of high aspect ratio. As could be observed in Figure 4.1 (e-f), VEG nanorod are firmly organized around the carbon fiber in the case of bf-VEG/CC. On the other hand, VEG nanorods are randomly distributed over the carbon fibers and wrapped in PVDF layer in the case of VEG/CC (Figure 4.2a). TEM image of VEG nanorod is shown in Figure 4.2b. Thermogravimetric analysis (TGA) clearly shows the decomposition of the organic component present in VEG at temperature of 225 ^{o}C (Figure 4.2c).

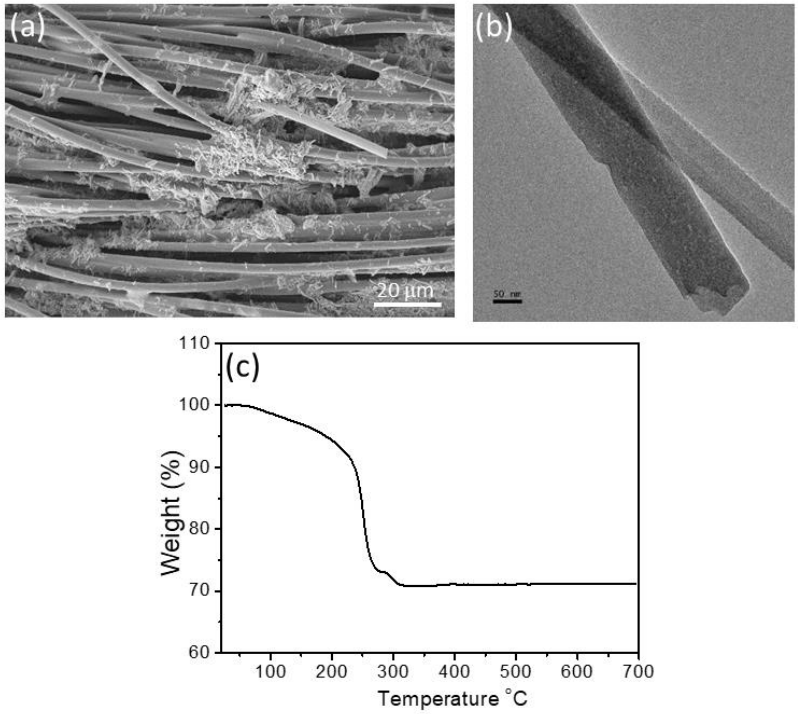

Figure 4.2 (a) FESEM image of (a) VEG/CC, (b) TEM image of VEG nanorod, and (c) TGA curve of VEG.

Figure 4.3a shows the CV profiles of bf-VEG/CC in 1 M $AlCl_3$ aqueous electrolyte at a scan rate of 2.5 mVs^{-1} in a voltage range of -0.3 V to 1 V (vs. Ag/AgCl). Clearly, redox activities are prominently noticeable. A pair of cathodic (peak A) and anodic (peak B) redox peaks are observed around 0.25 V and 0.50 V respectively. It appears that peak A may be a superimposition of two redox peaks. Similar redox activities are also observed in case of VEG/CC except peak $A^{/}$ seems to be composed of only one peak (Figure 4.3b). It is noted that the CV profiles in both the cases are highly reversible for the measured number of scans and it may be ascribed to continuous and

facile insertion/deinsertion of Al^{3+} ion in the VEG structure. This behavior is in contrast to the Zn^{2+} ion intercalation/ deintercalation phenomenon in VEG where two pairs of prominent cathodic and anodic redox peaks are always observed [14-15].

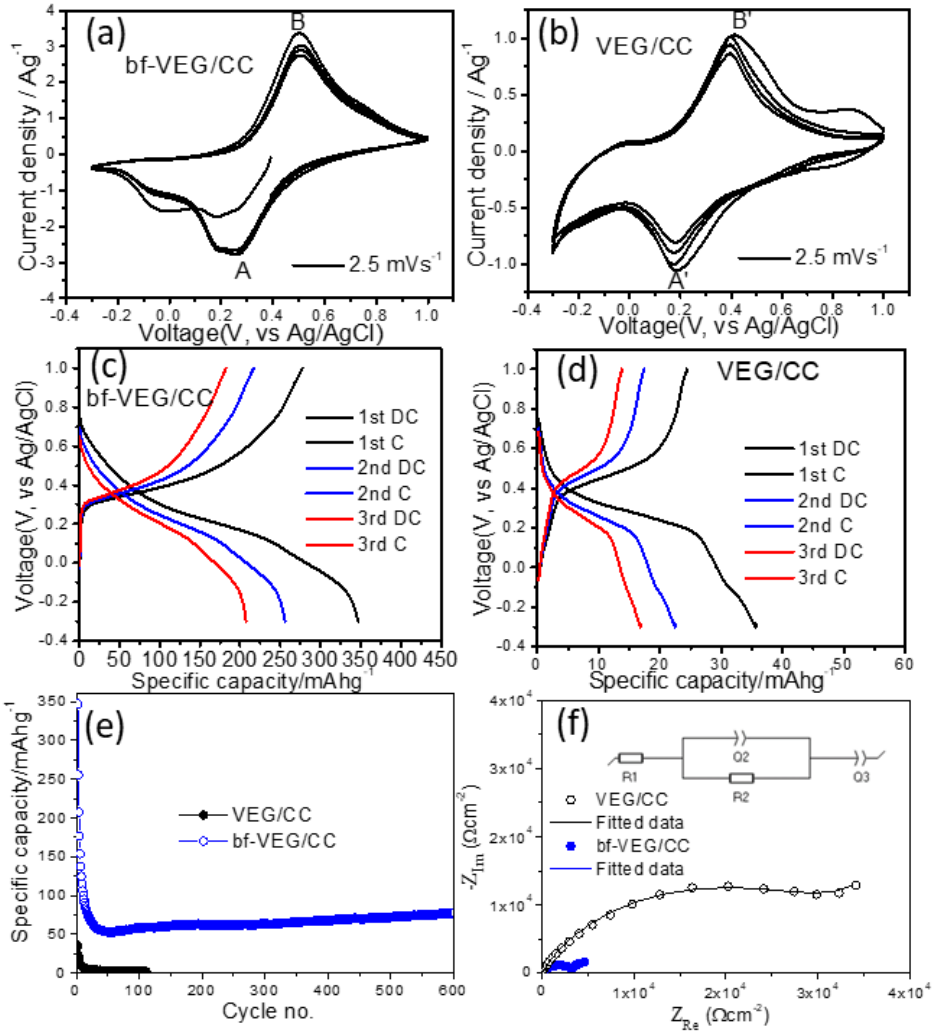

Figure 4.3 CV curves of (a) bf-VEG/CC, (b) VEG/CC at a scan rate of 2.5 mVs^{-1}. Galvanostatic discharge/charge curves of (c) bf-VEG/CC, (d) VEG/CC, (e) Comparison of discharge capacities with cycle number at a current density of 2 Ag^{-1}, and (f) EIS spectra for VEG/CC and bf-VEG/CC respectively. (Inset shows the equivalent circuit).

Galvanostatic charge/discharge profiles of bf-VEG and VEG are shown in Figure 4.3 (c, d) in 1 M $AlCl_3$ aqueous electrolyte at a specific current rate of 2 Ag^{-1}. As could be seen, there is no perfectly flat discharge/charge potential plateaus. Rather a short discharge plateau around 0.2 V could be noticed in both cases. Similarly, a small charge plateau around 0.34 V could be seen. The galvanostatic profiles are in

consistent with the respective CV profiles. The initial discharge and charge capacities of bf-VEG/CC were 346 $mAhg^{-1}$ and 277 $mAhg^{-1}$, which are much higher than the capacities obtained from VEG/CC (Figure 4.3d). The VEG/CC electrode delivered an initial discharge and charge capacities of only 35 $mAhg^{-1}$ and 24 $mAhg^{-1}$ at the identical current rate. The variation of discharge capacity with cycle number is shown in Figure 4.3e. It is obvious that the binder free electrode shows a superior cycling stability than VEG/CC. It is observed that binder free electrode could maintain a discharge capacity of 77 $mAhg^{-1}$ over 600 cycles at a specific current rate of 2 Ag^{-1} and even at high current rate of 2.5 Ag^{-1} (Figure 4.4), it could still deliver a discharge capacity around 41 mAg^{-1} over 500 cycles. On the contrary, pristine form of VEG shows negligible specific capacities (~2.3 $mAhg^{-1}$). This significant improvement in electrochemical performance may be attributed to the intimate electrochemical contact between the electrode and current collector, which is also supported by the EIS data. The EIS data are fitted with an equivalent circuit and it is shown in inset Figure 4.3f. It is found that the binder free electrode displays much lower charge transfer resistance (3.39 $k\Omega cm^{-2}$) than pristine VEG (32.95 $k\Omega cm^{-2}$). In order to get an assurance of correct estimation of specific capacities, CV and galvanostatic discharge/charge experiments were performed with the pristine form of carbon cloth in 1 M $AlCl_3$ aqueous electrolyte at identical current rate shown in Figure 4.5. These measurements rule out the possible electrochemical activity of the carbon cloth current collector. Therefore, it is certain that the electrochemical behavior is only due to VEG.

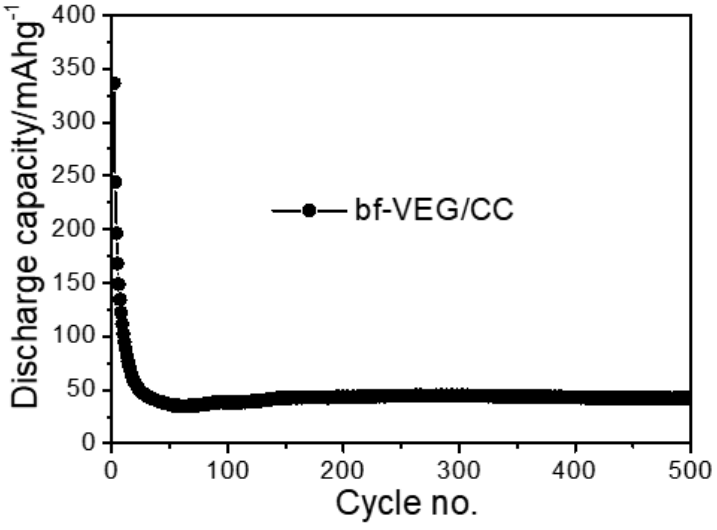

Figure 4.4 Variation of discharge capacity with cycle number at a current density of 2.5 Ag^{-1}.

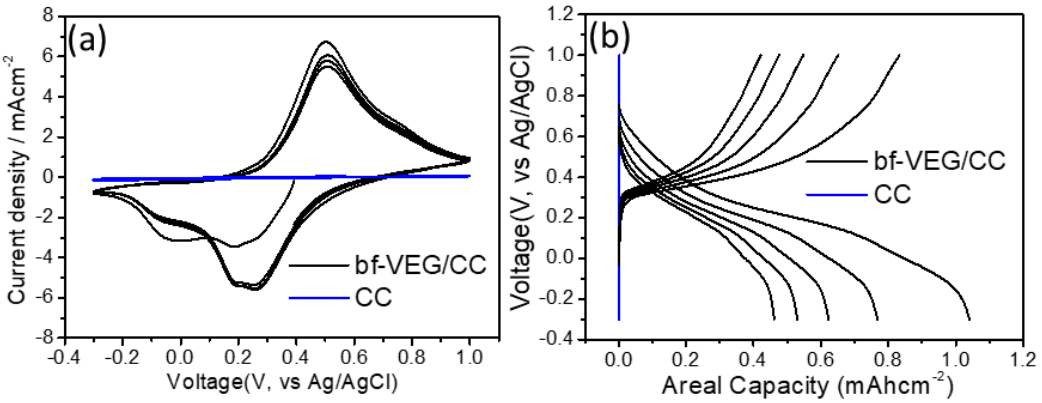

Figure 4.5 Comparison of (a) CV curves of pristine carbon cloth and bf-VEG/CC at a scan rate of 2.5 mVs^{-1}, and (b) galvanostatic discharge/charge curves pristine carbon cloth and binder free VEG/CC in 1 M $AlCl_3$ aqueous electrolyte at 2 Ag^{-1} current.

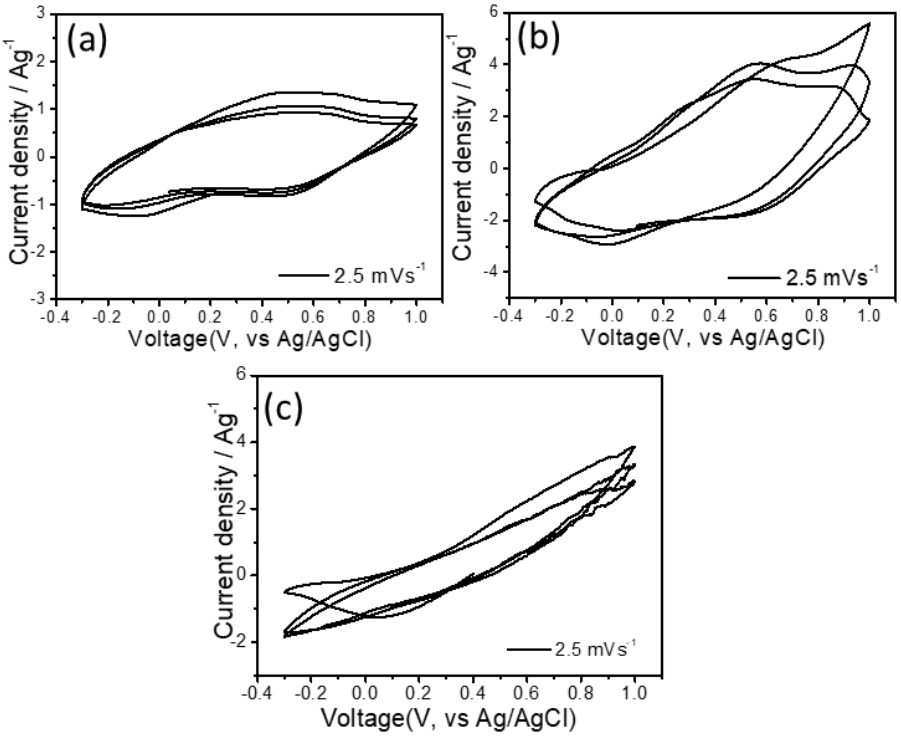

Figure 4.6 CV curves of bf-VEG/CC in (a) 1 M LiCl, (b) 1 M NaCl, and (c) 1 M $MgCl_2$ aqueous electrolytes at a scan rate of 2.5 mVs^{-1}.

For a comparison, CV experiments were also performed with binder free VEG electrode in 1 M LiCl, 1 M NaCl and 1 M $MgCl_2$ aqueous electrolytes at a scan rate of 2.5 mVs^{-1} which are shown in Figure 4.6. It is evident from the CV profiles that bf-VEG/CC shows a completely different behavior in Al^{3+} ion aqueous electrolyte than the rest of the investigated ions. There is no signature of prominent redox activities in these electrolytes unlike the case of Al^{3+} ion. Similar behavior was also observed for

MoO_3 and WO_3 [16-19]. A straightforward analysis is difficult here. The ionic radii of Li^+, Na^+, Mg^{2+} and Al^{3+} are 0.6 Å, 0.95 Å, 0.65 Å and 0.5 Å respectively [20]. It is tempting to infer that the Al^{3+} ion insertion process is easier since the ionic radius is smaller in case of Al^{3+} ion. However, since aqueous medium is used in the electrolyte, the metal ions are solvated by water molecules and, therefore, the effect of hydrated ions should not be ruled out. The hydrated radii of Li^+, Na^+, Mg^{2+} and Al^{3+} are 3.82 Å, 3.58 Å, 4.28 Å and 4.75 Å respectively [20]. Al^{3+} ion has the largest hydrated radius. It is unknown to us at this juncture how the hydrated ion communicates at the electrode-electrolyte interface. A detailed computational analysis is required to determine the hydration energies, the hydrodynamic behavior and the charge transfer process at the electrode-electrolyte interface in order to accurately understand this complex electrochemical process.

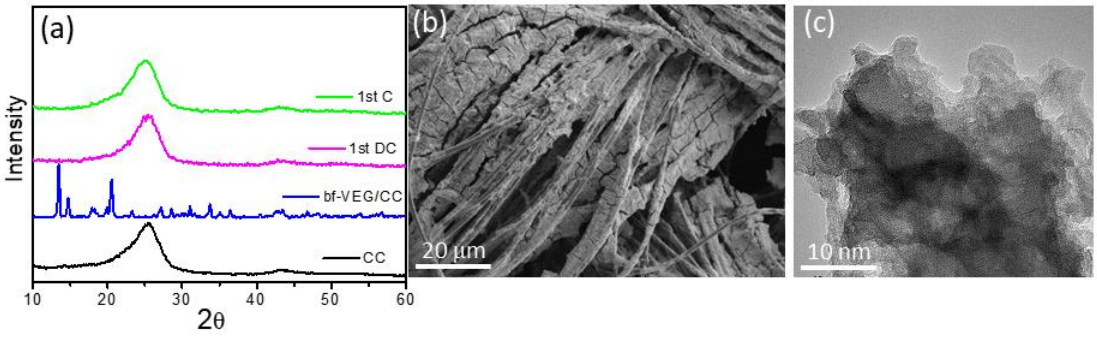

Figure 4.7 Ex-situ XRD patterns of bf-VEG/CC electrode before and after 1st discharge. (b-c) Ex-situ SEM and TEM images of bf-VEG/CC after 1st discharge.

In order to examine any possible structural and morphological changes of VEG during the electrochemical processes, post-mortem analysis of the electrodes was performed by spectroscopic and electron microscopic techniques. As shown in Figure 4.7a, the ex-situ XRD patterns indicate that there are no characteristic diffraction peaks of VEG in harvested VEG electrode after 1st discharge and 1st charge. The broad peak which appeared at $2\theta = 26.15^o$ is basically the characteristic diffraction peak of the carbon cloth. Ex-situ FESEM images (Figure 4.7b) also show a complete morphological change of the electrode after discharge. The one-dimensional VEG structure transformed to a polymeric layer type material after charge/discharge. Similarly, the ex-situ TEM analysis also indicates the complete loss of nanorod morphology and amorphous aggregated clusters could be noticed (Figure 4.7c). All these measurements signify the transformation of the crystalline VEG into an

amorphous phase after the Al^{3+} ion electrochemical processes. Ex-situ XPS was also conducted to probe the valence states of V 2*p* during the electrochemical processes. As shown in Figure 4.8a, the pristine VEG electrode exhibits two major peaks at 517.2 eV and 524.3 eV that are assigned to V $2p_{3/2}$ and V $2p_{1/3}$ components of V^{4+} [21]. However, after the 1st discharge state, the V2*p* shifted to lower energy suggesting the reduction of V^{4+} to V^{3+}. Similar behavior is observed after the 1st charge. This indicates that a mixed valence state exists in the electrochemical processes. Moreover, the appearance of Al 2*p* peak at 74.6 eV indicates presence of Al in the discharged electrode (Figure 4.8b). The presence of Al^{3+} ions in the discharged/charged state VEG electrode is also supported by the quantitative elemental mapping (Figure 4.9). The mapping shows presence of V, O, C and Al in the entire region. However, more Al is visible in the discharged electrode than the charged one (Figure 4.9e and Figure 4.9j). Furthermore, ex-situ Raman measurements of bf-VEG/CC were also performed in pristine state, after 1st discharge and 1st charge. For pristine VEG, six characteristics bands located at 139, 190, 280, 404, 689 and 987 cm^{-1} were observed (Figure 4.8c). After 1st discharge, the B_{3g} band at 139 cm^{-1} is observed to shift to 141.2 cm^{-1} (Figure 4.8d). Meanwhile, the band at 987 cm^{-1} and 689 cm^{-1}, ascribed to the stretching vibration of V-O mode also shifts to 990 cm^{-1} and 692 cm^{-1} (Figure 4.8e and Figure 4.8f). This shifting in Raman spectra could be related to the possible change in the bonding modes due to Al^{3+} ion insertion [22]. Further, to understand the Al^{3+} ion storage behavior, CV of bf-VEG/CC were performed at different scan rates in 1 M $AlCl_3$ aqueous electrolyte (Figure 4.10a). The diffusion controlled and capacitive controlled contributions are estimated using the following standard equations: $I= av^b$ and $I= k_1v + k_2v^{1/2}$, where I is the redox peak currents, a and b are adjustable parameters, v is the scan rate, k_1 and k_2 are constants [23-24]. Here, k_1v and $k_2v^{1/2}$ respectively correspond to the contributions arising out of capacitive controlled and diffusion-controlled processes. It is found that the diffusion-controlled process is the most dominating process (Figure 4.10b). For example, the olive color region shown in Figure 4.10c indicates the diffusion-controlled process at a scan rate of 2.5 mVs^{-1} which represents 83 % of the total capacity. The ratio of these contributions at various scan rates are displayed in Figure 4.10d. All these observations indicate possible Al^{3+} ion insertion and extraction in VEG. Based on these analysis, the following possible electrochemical reaction

mechanism may occur during initial discharge process: $VO(CH_2O)_2$ (crystalline) + $xAl^{3+} + 3xe^- \rightarrow (Al^{3+})_x[(V^{4+})_{(1-x)}(V^{3+})_x]O(CH_2O)_2$ (amorphous). It is noted here that a deterministic value of x is not possible at this juncture since the final composition is unknown and the ex-situ XRD pattern also could not be analyzed due to lack of any diffraction peaks. However, if all the V^{4+} states transform to V^{3+} states due to Al^{3+} ion insertion, then x = 1 which results in a theoretical capacity of 623 $mAhg^{-1}$. It is noted here that there is a possible dissolution of the electrode material in the electrolyte. The change of color of the electrolyte from transparent (before cycling) to green and yellow after cycling hints at it (Figure 4.11). Because of it, there may be a gradual decline of capacity during initial cycles. We harvested the electrolytes after 10^{th} and 200^{th} cycle and these were analyzed using UV-visible spectroscopy. An absorption band appears at 281 nm for 10^{th} cycle electrolyte. On the other hand, another new absorption band appears at 294 nm for 200^{th} cycle electrolyte. The exact physical origin of these peaks however could not be identified.

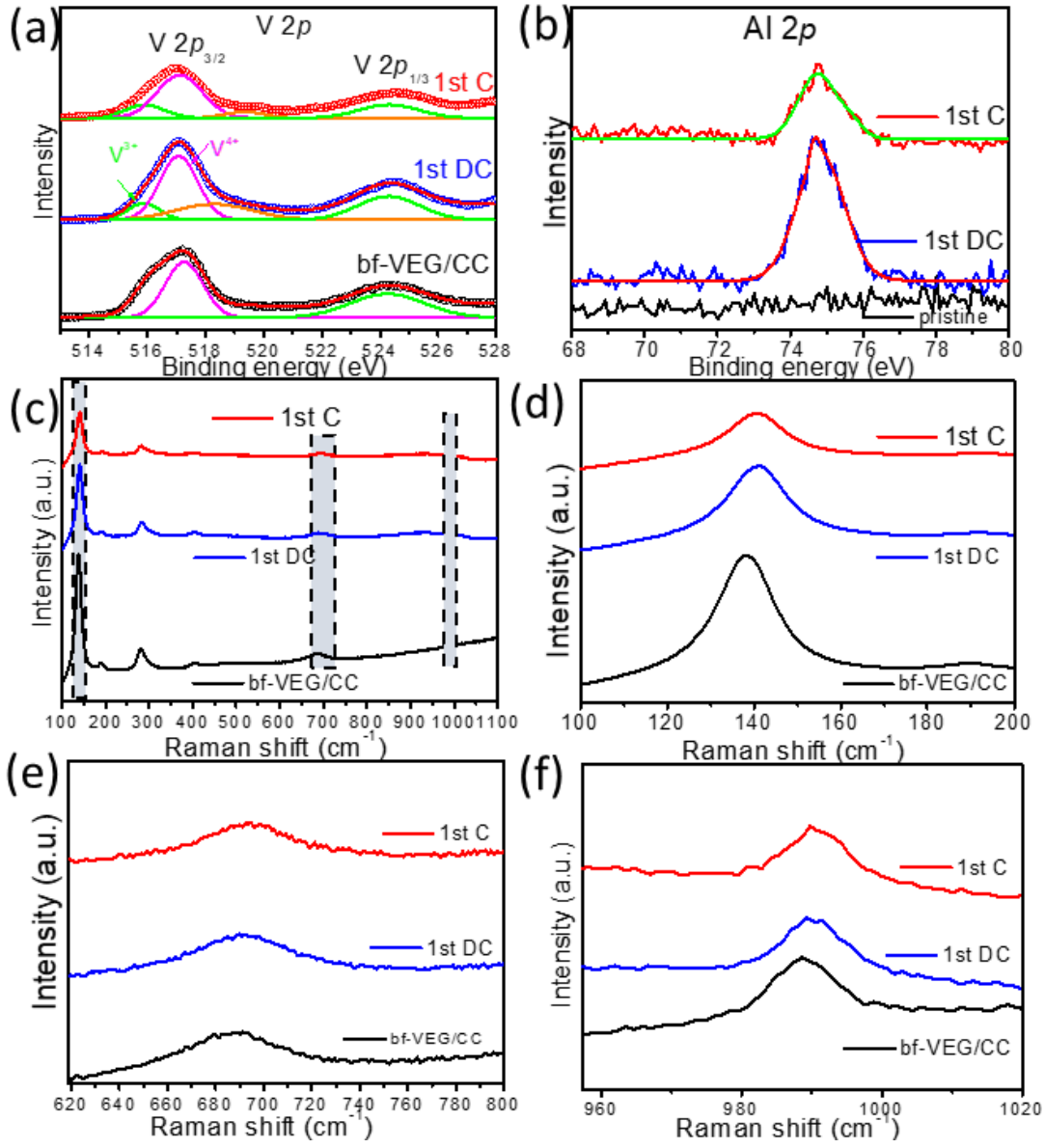

Figure 4.8 (a) Ex-situ XPS spectrum of V2*p* before discharge and after 1st discharge/1st charge state, (b) Ex-situ XPS spectrum of Al 2*p* before discharge and after 1st discharge/1st charge state, and (c) Ex-situ Raman spectra of bf-VEG/CC electrode before, after 1st discharge/1st charge state. (d-f) enlarged view of the dotted marked regions.

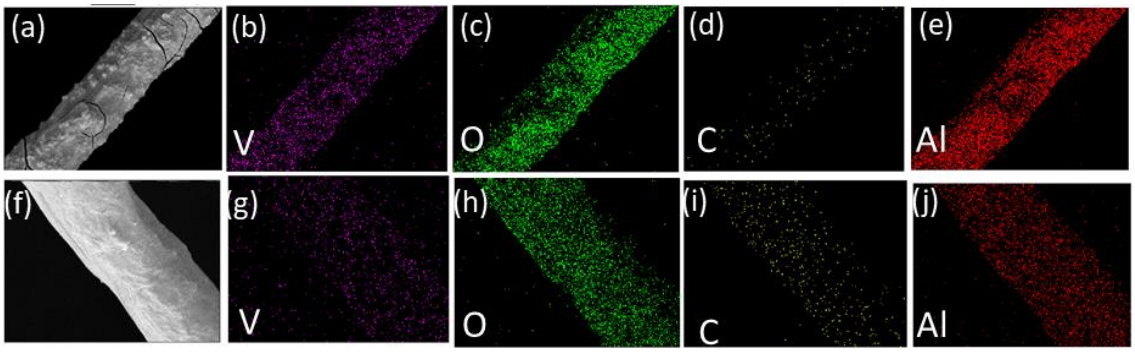

Figure 4.9 (a) SEM image of scanned area for elemental mapping of 1st discharge state binder free VEG/CC electrode. Elemental mapping images of (b) V, (c) O, (d) C and (e) Al of the 1st discharge state electrode. (f) SEM image of scanned area for elemental mapping of 1stcharge state bf-VEG/CC electrode Elemental mapping images of (g) V, (h) O, (i) C and (j) Al of the 1stcharge state electrode.

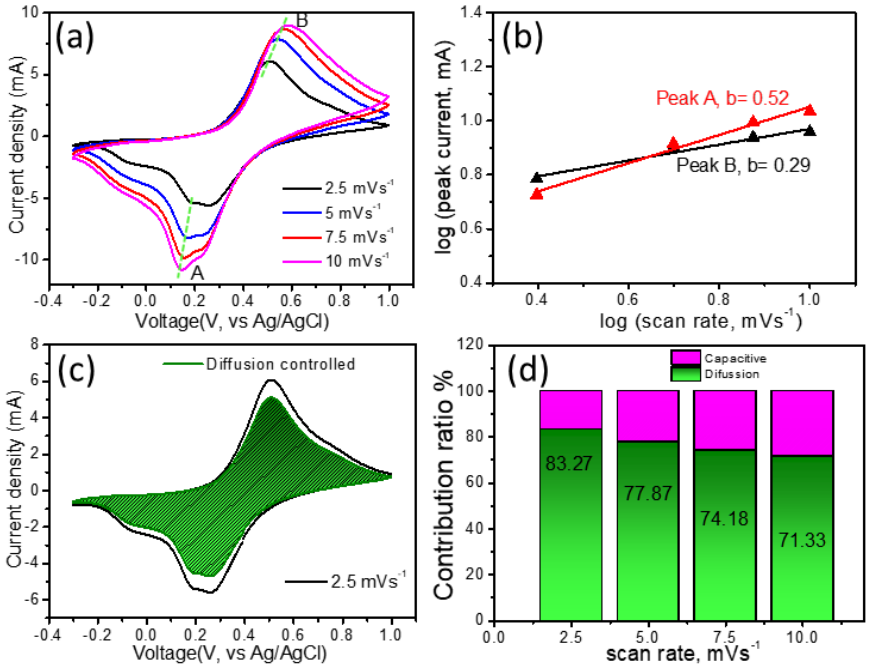

Figure 4.10 CV curves of bf-VEG/CC electrode at different scan rates, (b) corresponding log(i) vs log(v) plots, (c) CV curve with the diffusion-controlled contribution at a scan rate of 2.5 mVs^{-1}, and (d) contribution ratios of diffusion and capacitive-controlled at various scan rates in 1 M $AlCl_3$ aqueous electrolyte.

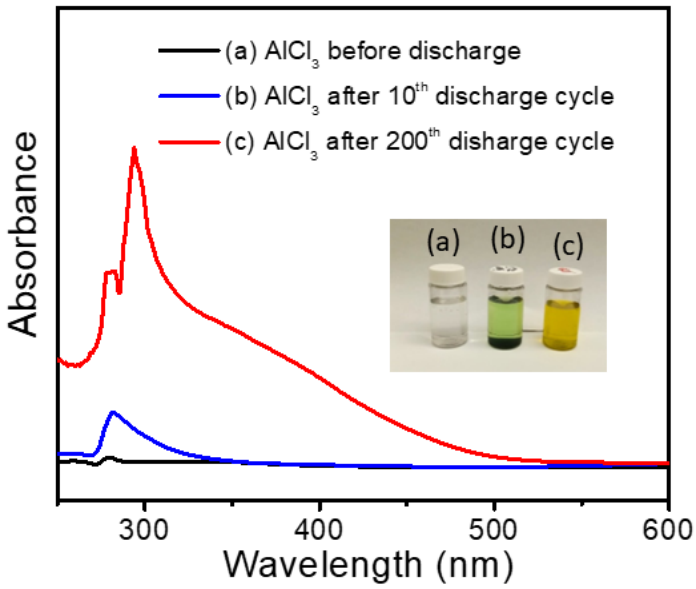

Figure 4.11 UV-visible spectra of the electrolyte before and after cycling. Inset Figure shows the digital image of the (a) pristine electrolyte, (b) harvested electrolyte after 10th cycle and (c) harvested electrolyte after 200th cycle.

4.4 Conclusion

In this chapter, a binder free VEG electrode is prepared and its electrochemical behavior for Al^{3+} ion storage in aqueous electrolyte is illustrated. The binder free electrode shows excellent long term cycling stability with specific capacity values of the order of 77 $mAhg^{-1}$ over hundreds of cycles which was not possible in pristine form of VEG. It was also found that diffusion-controlled process dominated the Al^{3+} ion storage behavior.

4.5 References

[1] Kim, Y., Park, Y., Kim, M., Lee, J., Kim, K.J., and Choi, J. W. Corrosion as the origin of limited lifetime of vanadium oxide-based aqueous zinc ion batteries. *Nat. Commun.*, 13:2371, 2022.

[2] Wang, Q., Xu, J., Zhang, W., Mao, M., Wei, Z., Wang, L., Cui, C., Zhu, Y., and Ma, J. Research progress on vanadium-based cathode materials for sodium ion batteries. *J. Mater. Chem. A* 6: 8815-8838, 2018

[3] Tang, H., Peng, Z., Wu, L., Xiong, F., Pei, C., An, Q., and Mai, L. Vanadium-based cathode materials for rechargeable multivalent batteries: challenges and opportunities. *Electrochem. Energy Rev.*, 1:169–199, 2018.

[4] Liu, Y., and Wu, X. Review of vanadium-based electrode materials for rechargeable aqueous zinc ion batteries. *J. Ener. Chem.,* 56: 223-237, 2021.

[5] Jayaprakash, N., and Das, S. K., Archer, L. A. The rechargeable aluminum-ion battery. *Chem. Commun.,* 47:12610, 2011.

[6] Liu, S., Pan, G. L., Li, G. R., and Gao, X. P. Copper hexacyanoferrate nanoparticles as cathode material for aqueous Al-ion batteries. *J. Mater. Chem. A,* 3: 959, 2015.

[7] Zhao, Q., Zachman, M. J., Al Sadat, W. I., Zheng, J. X., Kourkoutis, L. F., and Archer, L. Solid electrolyte interphases for high-energy aqueous aluminum electrochemical cells. *Sci. Adv.,* 4: eaau8131, 2018.

[8] Lahan, H., and Das, S. K. An approach to improve the Al^{3+} ion intercalation in anatase TiO_2 nanoparticle for aqueous aluminum-ion battery. *Ioni.,* 24: 1855, 2018.

[9] Kumar, S., Satish, R., Verma, V., Ren, H., Kidkhunthod, P., Manalastas Jr, W., and Srinivasan, M. Investigating $FeVO_4$ as a cathode material for aqueous aluminum-ion battery. *J. Power Sources,* 426:151– 161, 2019.

[10] Zhao, Q., Liu, L., Yin, J., Zheng, J., Zhang, D., Chen, J., and Archer, L. Proton intercalation/de-intercalation dynamics in vanadium oxides for aqueous aluminum electrochemical cells. *Angew. Chem.,* 59:3048-3052, 2020

[11] Weeks, C., Song, Y., Suzuki, M., Chernova, N. A., Zavalij, P.Y., and Whittingham, M. S. The one-dimensional chain structures of vanadyl glycolate and vanadyl acetate. *J. Mater. Chem.,* 13:1420-1423, 2003.

[12] Wang, X., Bi, X., Zheng, S., Wang, S., Zhang, Y., Du, H., and Lu, J. High-rate performance and ultralong cycle life enabled by hybrid organic–inorganic vanadyl ethylene glycolate for lithium-ion batteries. *Adv. Ener. Mater.,* 8:1801978, 2018.

[13] Li, Q., Zhu, Y., Yu, Y., and Qian, Y. Synthesis and transformation of vanadyl ethylene glycolate, and their applications in a lithium-ion battery. *Int. J. Electrochem. Sci.,* 7:5557 – 5564, 2012.

[14] Nagaraj, R., Pakhira, S., Aruchamy, K., Yadav, P., Mondal, D., Dharmalingm, K., Kotrappanavar, N. S., and Ghosh, D. Catalyzing the intercalation storage capacity of aqueous zinc-ion battery constructed with

Zn (II) preinserted organo-vanadyl hybrid cathode. *ACS Appl. Energy Mater.*, 3:3425, 2020

[15] Li, X., Feng, J., Wen, N., Chen, S., Kuang, Q., Fan, Q., Dong, Y., and Zhao, Y. High electrochemical performance of in-situ carbon-coated vanadyl ethylene glycolate as cathode for aqueous zinc-ion batteries. *Sol. State Ionic.*, 364:115632, 2021.

[16] Lahan, H., and Das, S. K. Al^{3+} ion intercalation in MoO_3 for aqueous aluminum-ion battery. *J. Power Sources*, 413: 134-138, 2019.

[17] Zhou, L., Yang, L., Yuan, P., Zou, J., Wu, Y., and Yu, C. α-MoO_3 Nanobelts: A High-performance cathode material for lithium-ion batteries. *J. Phys. Chem. C* 114: 21868–21872, 2010.

[18] Joseph, J., O'Mullane, A. P., and Ostrikov, K. Hexagonal molybdenum trioxide (h-MoO_3) as an electrode material for rechargeable aqueous aluminum-ion batteries. *ChemElectroChem.,* 6: 6002-6008, 2019.

[19] Lahan, H., and Das, S. K. Reversible Al^{3+} ion insertion into tungsten trioxide (WO_3) for aqueous aluminum-ion batteries. *Dalton Trans.*, 48: 6337-6340, 2019.

[20] Chao, D., Zhou, W., Xie, F., Ye, C., Li, H., Jaroniec, M., and Qiao, S. –Z., Roadmap for advanced aqueous batteries: from design of materials to applications, *Sci. Adv.*, 6: eaba4098, 2020.

[21] González, J. R., Nacimiento, F., Cabello, M., Alcántara, R., Lavela, P., and Tirado, J. L. Reversible intercalation of aluminum into vanadium pentoxide xerogel for aqueous rechargeable batteries. *RSC Adv.*, 6(67):62157-62164, 2016.

[22] Zhao, Q., Zachman, M. J., Sadat, W. I. Al., Zheng, J., Kourkoutis, L. F., and Archer, L. Solid electrolyte interphases for high-energy aqueous aluminum electrochemical cells. *Sci. Adv.*, 4:8131, 2018.

[23] Brezesinski, T., Wang, J., Tolbert, S. H., and Dunn, B., Ordered mesoporous α-MoO_3 with iso-oriented nanocrystalline walls for thin-film pseudocapacitors. *Nat. Mater.*, 9: 146, 2010.

[24] Wang, J., Polleux, J., Lim, J., and Dunn, B. Pseudocapacitive contributions to electrochemical energy storage in TiO_2 (anatase) nanoparticles. *J. Phys. Chem. C*, 111:14925-14931, 2007.